Synthesis, structure, and magnetism in the ferromagnet La₃MnAs₅: Well-separated spin chains coupled via itinerant electrons

L. Duan,[1,2] X. C. Wang ⬤,[1,3,*] J. Zhang,[1,3] Z. Hu,[4] J. F. Zhao,[1,3] Y. G. Feng,[2] H. L. Zhang,[2] H.-J. Lin,[5]
C. T. Chen,[5] W. Wu ⬤,[6] Z. Li,[7] R. Wang,[8] J. F. Zhang,[1,†] T. Xiang,[1,3] and C. Q. Jin[1,3,9,‡]

[1]*Beijing National Laboratory for Condensed Matter Physics, Institute of Physics, Chinese Academy of Sciences, Beijing 100190, China*
[2]*School of Materials Science and Engineering, Henan University of Technology, Zhengzhou 450007, China*
[3]*School of Physics, University of Chinese Academy of Sciences, Beijing 100190, China*
[4]*Max Plank Institute for Chemical Physics of Solids, Nothnitzer Strasse 40, D-01187 Dresden, Germany*
[5]*National Synchrotron Radiation Research Center, Hsinchu 30076, Taiwan*
[6]*Institute for Materials Discovery, University College London, Malet Place, London WC1E 7JE, United Kingdom*
[7]*College of Materials Science and Engineering, Nanjing University of Science and Technology, Nanjing 210094, China*
[8]*Institute for Structure and Function and Department of Physics, Chongqing University, Chongqing 400044, China*
[9]*Materials Research Lab at Songshan Lake, Dongguan 523808, China*

In this work, we systematically report the synthesis, structure, and magnetism of a compound of filled anti-Mn₃Si₅ type La₃MnAs₅. It crystallizes in a hexagonal structure with the space group of $P6_3/mcm$ (193). The structure consists of face-sharing MnAs₆ octahedral chains along the c axis, which are well separated by a large distance of 8.9913 Å, demonstrating a strong one-dimensional (1D) structural character. Physical property measurements indicate that La₃MnAs₅ is a ferromagnetic metal with $T_C \sim 112$ K. Due to the short-range intrachain spin coupling, the susceptibility deviates from the Curie-Weiss behavior in a wide temperature window and the magnetic entropy corresponding to the ferromagnetic transition is significantly lower than that expected from the fully saturated state. The magnetic critical behavior studies show that La₃MnAs₅ can be described by the three-dimensional Heisenberg model. The orbital hybridization between the 1D MnAs₆ chain and intermediate La atom near the Fermi level reveals that the itinerant electrons play a key role in transmitting spin interaction among the MnAs₆ spin chains. Our results indicate that La₃MnAs₅ is a rare ferromagnetic metal with well-separated spin chains, which provides a good opportunity to study the mechanism of interchain spin coupling via itinerant electrons.

I. INTRODUCTION

Quasi-one-dimensional (1D) systems exhibit rich physical phenomena which are drastically different from high–dimensional ones [1]. For an ideal 1D spin chain, no long-range magnetic order can exist at finite temperature as implied in the Mermin-Wagner theorem [2]. On the other hand, for a quasi-1D spin chain system, although the interchain coupling is generally much weaker than intrachain couplings, it plays a key role in the formation of the long-range spin order (LRSO) [3]. Far above the LRSO transition temperature, short-range spin orders (SRSOs) associated with the intrachain spin correlation have been developed gradually, which leads to many exotic physics, such as invisible specific heat jump corresponding to the LRSO formation in the spin chain compound Ba₆Cr₂S₁₀ because most of the magnetic entropy has been released due to the formation of SRSOs [4].

To tailor the three-dimensional (3D) magnetism of quasi-1D spin chains, monatomic transition-metal oxide chains have been reported to be deposited on the surface of nonmagnetic metals Ir and Pt, and the spin chains are found to be coupled via the interaction exchange with itinerant electrons, the so-called Ruderman-Kittel-Kasuya-Yosida (RKKY) interaction, to form chiral spin order [5,6]. Besides the artificial spin chains coupled via RKKY interaction, the filled anti-Mn₃Si₅ type ternary compounds A_3MX_5 (A = Ba or La; M = transition metal; X = chalcogen or pnictogen) provide a unique opportunity to explore the magnetism of 1D spin chains in bulk materials [7–17]. A_3MX_5 consists of face-sharing MX_6 octahedral chains along the c axis, which are arranged with a triangular configuration in the ab plane and separated by A and X ions with a significant large distance of ∼9 Å, presenting strongly 1D structure character. For a Ba₃MX_5 system, most of the compounds exhibit insulating behavior [4,10–15]. The electron hopping between MX_6 chains is small, leading to a weak interchain coupling and thus a very low LRSO transition temperature [4,10,13]. For example, the trimerized Ba₉V₃Se₁₅ featured with 1D ferromagneticlike spin chain has been reported to undergo a LRSO transition at 2.5 K [13]. On the contrary, all the reported

*wangxiancheng@iphy.ac.cn
†zjf@iphy.ac.cn
‡jin@iphy.ac.cn

La_3MX_5 compounds are metallic because the contribution of La^{3+} to the density of states (DOS) at the Fermi level cannot be ignored [7,9,18–20]. The conducting MX_6 chains are bridged by La^{3+} to form a 3D metal, which should greatly enhance the interchain electron hopping and thus the interchain spin coupling. Such as in La_3CrAs_5, the LRSO ferromagnetic temperature has been increased to 50 K due to the 3D metallic property. In spite of the metallic nature, La_3CrAs_5 still exhibits 1D spin chain behavior; the magnetic susceptibility above T_C deviates from the Curie-Weiss (CW) law in a wide temperature range due to the SRSOs formation [7]. Under the synergistic action between the direct magnetic exchange and the itinerant electron mediated indirect spin exchange, a ferromagnetism with chiral XY type magnetic critical behavior was suggested in La_3CrAs_5 [8].

The high-pressure technique is a powerful tool to explore alternative functional materials [4,21–23]. Here, we report the discovery of a unique material La_3MnAs_5 under high-pressure conditions, which consists of face-sharing $MnAs_6$ chains. The electrons in the La-5d, Mn-3d, and As-4p orbitals contribute to the DOS near the Fermi level and thus lead to a metallic behavior in La_3MnAs_5. The spin chains of $MnAs_6$ octahedrons are coupled via itinerant electrons to form a long-range ferromagnetic order with greatly enhanced $T_C \sim 112$ K. In addition, the magnetic critical behavior of La_3MnAs_5 can be described within the framework of the 3D Heisenberg universality class.

II. EXPERIMENTS AND CALCULATIONS

A polycrystalline sample of La_3MnAs_5 was synthesized under the conditions of high pressure and high temperature. Commercially available lumps of La (Alfa, >99.99% pure), lumps of As (Alfa, >99.999% pure), and Mn powder (Alfa, >99.99% pure) were used as the starting materials. The precursor LaAs was prepared by the reaction of La and As at 700 °C in an evacuated quartz tube. The obtained LaAs, Mn, and As were mixed according to the elementary ratio of stoichiometric La_3MnAs_5, pressed into a pellet with a diameter of 6 mm, then subjected to high-pressure synthesis under 5.5 GPa pressure and 1400 °C for 40 min in a cubic anvil type high-pressure apparatus, of which the details have been reported in Refs. [21,24].

The x-ray diffraction was conducted on a Rigaku Ultima VI (3 KW) diffractometer using Cu $K\alpha$ radiation generated at 40 kV and 40 mA. The Rietveld refinements for the diffraction patterns were performed using GSAS software packages. The magnetic measurements were carried out using a superconducting quantum interference device (SQUID). The resistivity and specific heat measurements were performed on a physical property measuring system (PPMS). Soft x-ray absorption scattering (XAS) at the Mn $L_{2,3}$ edges was measured at the beamline BL11A of the National Synchrotron Radiation Research Center (NSRRC) in Taiwan.

The fully spin-polarized electronic structure was calculated based on the density functional theory (DFT) [25,26] as implemented in the QUANTUM ESPRESSO (QE) package [27]. The interactions between electrons and nuclei were described by the ultrasoft pseudopotentials [28]. The generalized gradient approximation (GGA) of Perdew-Burke-Ernzerhof (PBE)

type [29] was chosen for the exchange-correlation functional. The kinetic energy cutoffs of the wave function and charge density were set to be 100 and 1000 Ry, respectively. A $8 \times 8 \times 12$ k-point mesh was used for the Brillouin zone (BZ) sampling. The Gaussian smearing method with a width of 0.004 Ry was employed for the Fermi surface broadening. In structural optimization, both lattice constants and internal atomic positions were fully relaxed until the forces on all atoms were smaller than 0.002 Ry/bohr. Our optimal lattice constants are $a_0 = 8.97$ Å and $c_0 = 5.96$ Å, which well agrees with the experimental measurements. The electronic correlation effect among Mn 3d electrons was incorporated by using the $GGA + U$ formalism of Dudarev *et al.* [30]. The effective Hubbard U on Mn^{2+} is empirically set as 4 eV, in the range of 3–5 eV of previous studies on other Mn^{2+} compounds [31–33].

III. RESULTS

A. Structure and phase transition

Figure 1(a) shows the x-ray diffraction pattern for La_3MnAs_5. All the peaks can be indexed using a hexagonal structure with the lattice parameters of $a = b = 8.9913(1)$ Å and $c = 5.9416(1)$ Å. Here, the structure of La_3TiSb_5, crystallizing into the space group of $P6_3/mcm$ (193), was adopted as the initial model to carry out the refinement for the x-ray diffraction data [34]. The refinement smoothly converges to $R_{wp} = 5.3\%$, $R_p = 3.4\%$, and $\chi^2 = 3.76$. The crystallographic data are obtained and summarized as shown in Table I. The sketch of La_3MnAs_5 crystal structure is shown in Figs. 1(b) and 1(c), viewed with the projection along the c axis and along the [100] direction, respectively. The crystal structure contains the face-sharing $MnAs_6$ octahedral chains along the c axis, which are arranged triangularly in the ab plane. In the $MnAs_6$ chains, the bonding length of Mn-As is 2.6735 Å and the bond angle of Mn-As-Mn is 67.5°. These $MnAs_6$ chains are separated by La and As atoms with a significantly large interchain distance about 8.9913 Å, while the distance between adjacent Mn ions in the chain is 2.9708 Å, thus exhibiting a strongly 1D structure character.

The oxidation state of Mn ions in La_3MnAs_5 was investigated by XAS at the Mn-$L_{2,3}$ edge together with MnO, $LaMnO_3$ [35] and $SrMnO_3$ [36,37] as Mn^{2+}, Mn^{3+}, and Mn^{4+} reference materials, respectively, as shown in Fig. 2. One can see that the spectrum weight shifts toward high energy with the increase of oxidation state of Mn. La_3MnAs_5 and MnO have the same energy position at the Mn-L_2 and Mn-L_3 edges, but La_3MnAs_5 shows fewer multiplet spectral features, which implies that the oxidation state of Mn in La_3MnAs_5 is +2 and partial electrons in the Mn-3d orbital is delocalized similar to the situation in LaMnPO [38].

Figure 3(a) displays the resistivity $\rho(T)$ of La_3MnAs_5 measured within the temperature range from 2 to 300 K, which exhibits a metallic behavior with the room-temperature resistivity ρ (300 K) ~ 2.2 mΩ cm. The metallic state is expected for the La_3MX_5 system since La^{3+} in general has nonzero density of states (DOS) at the Fermi level; the following calculations will further confirm the result. In addition, there is an anomaly at ~ 112 K in the resistivity curve, below which the

TABLE I. The summary of the crystallographic data at room temperature for La_3MnAs_5.

Compound	La_3MnAs_5				
Space group: $P6_3/mcm$—hexagonal (No. 193)					
$a=$ 8.9913(1) Å $c=$ 5.9416(1) Å					
$V =$ 415.99(1) Å³ $Z = 2$					
$\chi^2 =$ 3.76; $R_p =$ 3.4%; $R_{wp} =$ 5.3%					
Site	Wyckoff	x	y	z	$100U$ (Å)
La	6g	0.6233(6)	0	1/4	1.31
Mn	2b	0	0	0	0.58
As(1)	6g	0.2472(3)	0	1/4	0.87
As(2)	4d	1/3	2/3	0	3.22
Mn-As	2.6735(3) Å		Mn-Mn (intra)		2.9708(1) Å
Mn-Mn (inter)	8.9913(1) Å		Mn-As-Mn	67.5(1)°	

resistivity decreases rapidly. The anomaly temperature also can be clearly evidenced by the sharp increase of the steplike temperature derivative of resistivity $d\rho/dT$. This hints that a phase transition occurs there.

The temperature dependence of magnetic susceptibility for La_3MnAs_5 measured with $H = 1000$ Oe is shown in Fig. 3(b). The field-cooling (FC) and zero field cooling (ZFC) curves are overlapped in the whole measured temperature range. The susceptibility increases sharply at $T_C \sim 112$ K, exhibiting a ferromagnetic transition. The inverse susceptibility $1/\chi$ vs temperature is presented in Fig. 3(b) as well. In the high-temperature range of 200–300 K, $1/\chi(T)$ displays a straight line, suggesting that the susceptibility follows the CW law $\chi^{-1} = (T - T_\theta)/C$, where T_θ is the Weiss temperature and C is the Curie constant, while the susceptibility below 170 K deviates gradually from the line, which should arise from the SRSOs formation associated with the intrachain spin coupling. After linearly fitting the high-temperature data, the Weiss temperature T_θ is estimated to be 123 K, which is 11 K larger than T_C; the positive value confirms that the dominant interaction is ferromagnetic. The effect moment μ_{eff} is calculated to be 4.33 μ_B/Mn, corresponding to the local spin $S = 3.4/2$, which is much smaller than the expected for Mn^{2+} with $S = 5/2$. This implies that some of the 3d electrons are itinerant, which is consistent with the results from our XAS experiments. The inset of Fig. 3(b) shows the magnetic hysteresis curves measured at 2 K. The saturation magnetization μ_{sat} is about 1.8 μ_B per Mn, which is reduced relative to the local spin of $S = 3.4/2$. The reduced ordered moment is a comment phenomenon for a quasi-1D spin chain system due to the strong quantum spin fluctuation.

The specific heat $C(T)$ curve of La_3MnAs_5 measured between 2 and 200 K under zero magnetic field is presented in Fig. 3(c). Obviously, there is a small peak at $T_C \sim 112$ K, which is consistent with the resistivity and susceptibility data, further confirming the phase transition. In order to extract the magnetic contribution C_m associated with this transition, we fit the specific heat data to obtain the lattice contribution with the Thirring model [39]: $C_{lat} = 3NR(\sum_{n=1}^{\infty} b_n\mu^{-n})$, where N is the number of atoms in the unit cell, R is the idea gas constant, $\mu = (2\pi T/\theta_D)^2 + 1$, and θ_D is the Debye temperature. This model can achieve an accuracy of $\sim$0.03% with only four

terms for a Debye solid at $T = \theta_D/4$. In our case, we use $n = 4$ and obtained a reasonable accuracy as demonstrated by the blue curve in Fig. 3(c). After subtracting the contribution of lattice, the magnetic contribution C_m can be obtained, as seen in the set of Fig. 3(c). The temperature dependence of C_m exhibits a sharp peak at the $T_C^{SH} \sim 112$ K. Finally, we can obtain the magnetic entropy through the integration of C_m/T. The total magnetic entropy change ΔS caused by the long-range ordering transition is $\sim$0.8 J/mol K, which is only $\sim$9.5% of the expected value $R\text{Ln}(2S + 1) = 8.5$ J/mol K; here the ordered spin $S = 1.8/2$ is used. This suggests that most of the magnetic entropy has been released above T_C due to the formation of SRSOs. Therefore, both the magnetic data and the specific heat data indicate that La_3MnAs_5 has the properties of quasi-1D spin chains although it is a 3D metal. Due to the metallic state, the $MnAs_6$ chains are coupled via itinerant electrons although they are separated by a large distance, which leads to a moderate interchain spin coupling and greatly enhances the long-range ferromagnetic transition temperature. This situation is similar to the diluted magnetic semiconductor (DMS) [40–42], where the diluted magnetic ions doped in the DMS are coupled with the help of free charge carriers to form long-range magnetic order.

B. Critical behavior

Now we will turn to the study of the magnetic critical behavior for La_3MnAs_5 since it is an efficient method to help us to understand the magnetism. For a magnetic transition, the critical exponents are usually used to identify the critical behavior. In the vicinity of a second-order FM transition, the spontaneous magnetization $M_s|_{H=0}$ and initial magnetic susceptibility $\chi|_{H=0}$ display power law dependence on the reduced temperature $\varepsilon = |T - T_C|/T_C$ with the critical exponents of β and γ. In addition, just at the critical temperature T_C, $M(H)$ is power law dependent on magnetic field H with the critical exponents of $1/\delta$. That is [43,44],

$$M|_{H=0} \sim \varepsilon^\beta \ (T < T_C), \tag{1}$$

$$\chi^{-1}|_{H=0} \sim \varepsilon^\gamma \ (T > T_C), \tag{2}$$

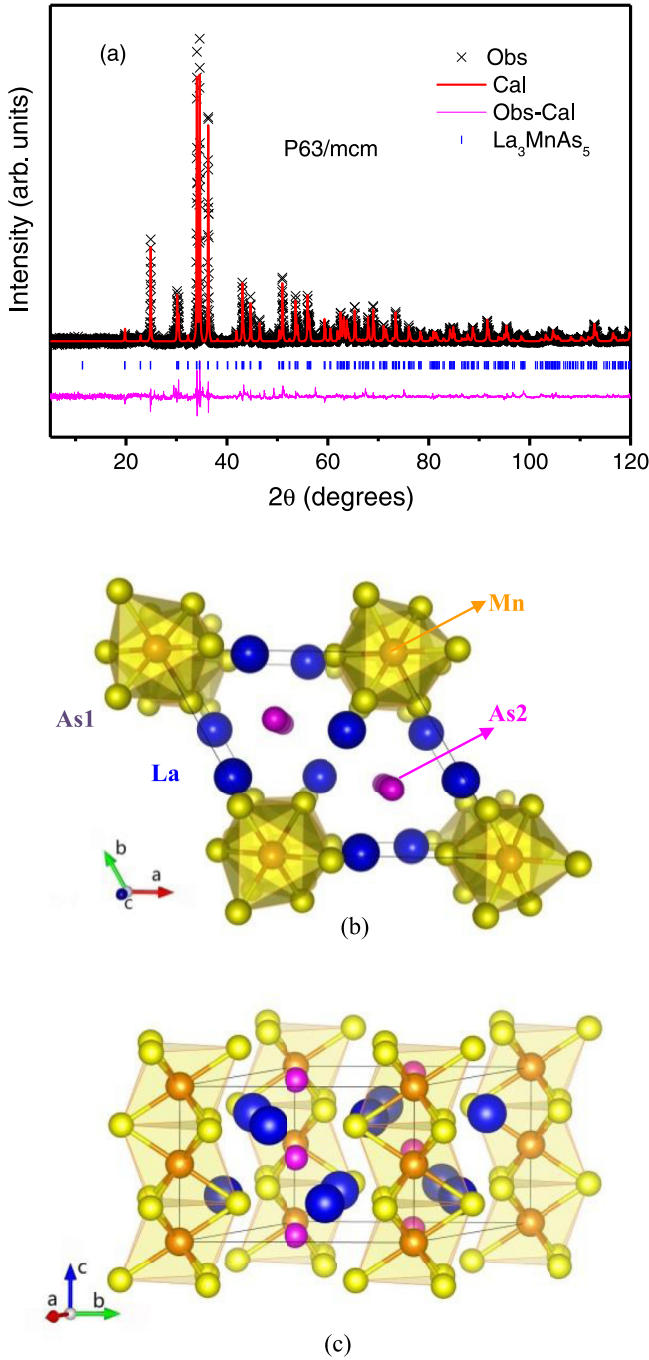$$M(H) \sim H^{1/\delta} \ (T = T_C). \tag{3}$$

FIG. 1. (a) The powder x-ray diffraction pattern of La_3MnAs_5 and the refinement with the space group of $P6_3/mcm$ (193). (b), (c) The sketch of the crystal structure of La_3MnAs_5 viewed with the projection along the c axis and [100] direction, respectively, showing the triangular lattice configuration and chain structure character.

FIG. 2. The Mn-$L_{2,3}$ XAS spectra of La_3MnAs_5 together with MnO, $LaMnO_3$, and $SrMnO_3$ as Mn^{2+}, Mn^{3+}, and Mn^{4+} references, respectively.

which covers the ferromagnetic transition. These isothermal magnetization data were replotted in the Arrott plots M^2 vs H/M, as shown in Fig. 4(b). According to the mean-field model, the M^2 vs H/M curves should be a series of parallel straight lines under high field. However, all the curves in the Arrott plots here are unambiguously nonlinear, ruling out the possibility of the mean-field model. However, from the positive slopes of the M^2 vs H/M curves we can speculate that the ferromagnetic transition in La_3MnAs_5 is a second-order one according to the criterion suggested by Banerjee [46]. Since the mean-field model is invalid here, a modified Arrott plot should be employed to obtain the critical exponents. In Figs. 5(a)–5(c), the modified Arrott plots $M^{1/\beta}$ vs $(H/M)^{1/\gamma}$ are plotted with the critical exponents of the 3D Heisenberg model, 3D XY model, and 3D Ising model. All three models exhibit quasistraight lines in the high-field region. The normalized slopes (NS) defined as $NS = S(T)/S(T_C)$ (here $T_C \sim 112$ K) enables one to identify the most suitable model by comparing the NS with the ideal value of unity. Figure 5(d) shows the plots of NS vs T for the three different models, which indicates that the Heisenberg model is the most appropriate to describe the critical behavior of La_3MnAs_5.

To determine precisely the critical exponents, an iterative process was employed [47]. Starting from the modified Arrott plots with the Heisenberg model ($\beta = 0.365$ and $\gamma = 1.386$), we can get the spontaneous magnetization $M_s(T)$ and the inverse of initial magnetic susceptibility $\chi_0^{-1}(T)$ from the intersections of the linear extrapolation line with the $M^{1/\beta}$ and the $(H/M)^{1/\gamma}$ axis, respectively. By fitting the $M_s(T)$ and $\chi_0^{-1}(T)$ data with Eqs. (1) and (2), we can obtain the new critical exponents of β and γ, which we can use to construct new the modified Arrott plots $M^{1/\beta}$ vs $(H/M)^{1/\gamma}$ until the expo-

Different critical behaviors can be determined with sets of critical exponents, which are derived from several theory models, for example, $\beta = 0.364$ and $\gamma = 1.386$ for the 3D Heisenberg model [45].

Here, the critical exponents for La_3MnAs_5 were obtained by the modified Arrott plot, Kouvel-Fisher method, and critical isotherm analysis. Figure 4(a) presents the isothermal magnetization curves of La_3MnAs_5 between 101 and 118 K,
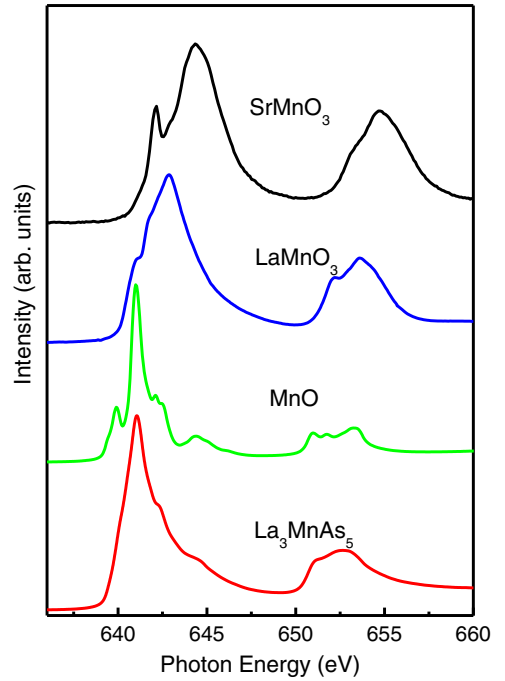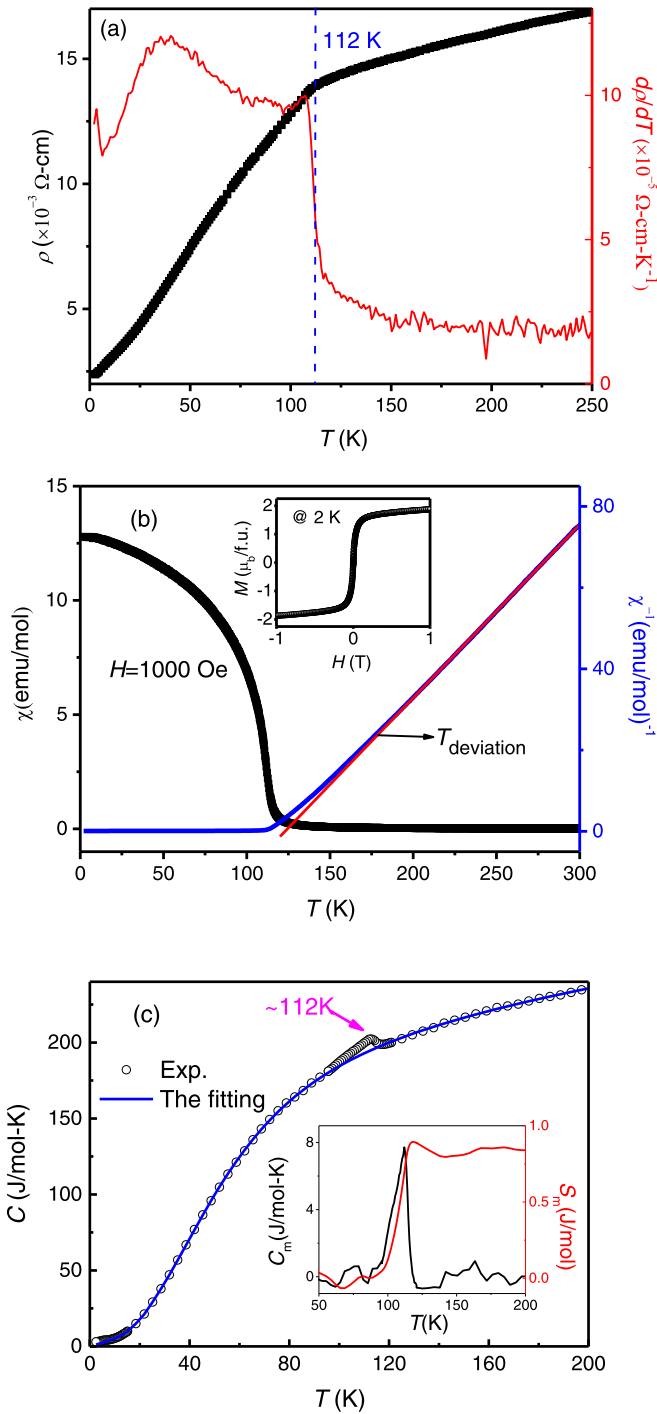
FIG. 3. (a) The temperature dependence of resistivity of La$_3$MnAs$_5$. (b) The magnetic susceptibility and the reverse susceptibility vs temperature. The red line is the fit using the CW equation between 200 and 300 K. The inset is the magnetic hysteresis curve measured at 2 K. (c) The temperature dependence of specific heat. The blue line is the fitting by the Thirring model. The inset shows the magnetic contribution to the specific heat and the magnetic entropy corresponding to magnetic transition.

FIG. 4. (a) Isothermal magnetization (M vs H) curves between 101 and 118 K of La$_3$MnAs$_5$. (b) Arrott plots M^2 vs H/M.

obtained values of critical exponents are very close to that of the Heisenberg model.

In addition, the critical exponents as well as T_C also can be determined by Kouvel-Fisher relations [44]:

$$M_s(T)/[dM_s(T)/dT] = (T - T_c)/\beta, \tag{4}$$

$$\chi_0^{-1}(T)/[d\chi_0^{-1}(T)/dT] = (T - T_c)/\gamma, \tag{5}$$

where the $M_s(T)$ and $\chi_0^{-1}(T)$ data are obtained from the final modified Arrott plots. The Kouvel-Fisher plot is displayed in Fig. 6(b). The temperature dependence of $M_s/(dM_s/dT)$ and $\chi_0^{-1}/(d\chi_0^{-1}/dT)$ exhibit straight lines, to which the linear fittings yield $\beta = 0.386(4)$ with $T_C^- \sim 108.3(2)$ K and $\gamma = 1.408(1)$ with $T_C^+ \sim 108.2(1)$ K. These values of critical exponents and T_C agree well with the results from the iterative method.

Besides β and γ, another critical exponent δ can be deduced via Eq. (3) [43,44]. Figure 7 shows the isothermal magnetization at 108 K, and the inset shows the plot on the logarithmic scales. The $\ln(M)$ vs $\ln(H)$ plot displays a straight line. The critical exponent δ can be estimated to be 4.83 by the linear fitting. It should be noted that the critical exponent δ is not an independent exponent. It also can be directly calculated according to the Widom scaling relation $\delta = 1 + \gamma/\beta$ [48]. Here, the values of β and γ obtained from the Kouvel-Fisher method are used for the calculation, and the calculated value of δ is 4.54, which is consistent with the value determined from Fig. 7.

To further confirm the validity of the above analysis about the critical exponents and T_C, we can check whether these values follow the scaling equation. According to the scaling

nents are converged. Figure 6(a) presents the itinerant process and the converged critical exponents $\beta = 0.362(6)$ with $T_C^- = 108.2(1)$ K and $\gamma = 1.379(2)$ with $T_C^+ = 108.1(1)$ K. The
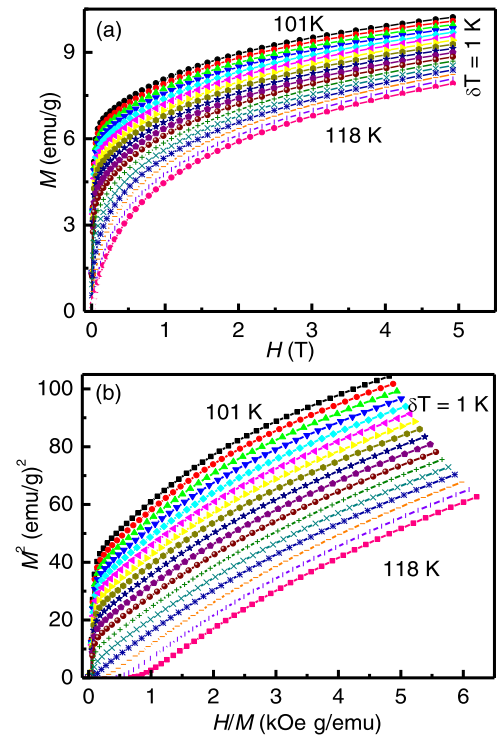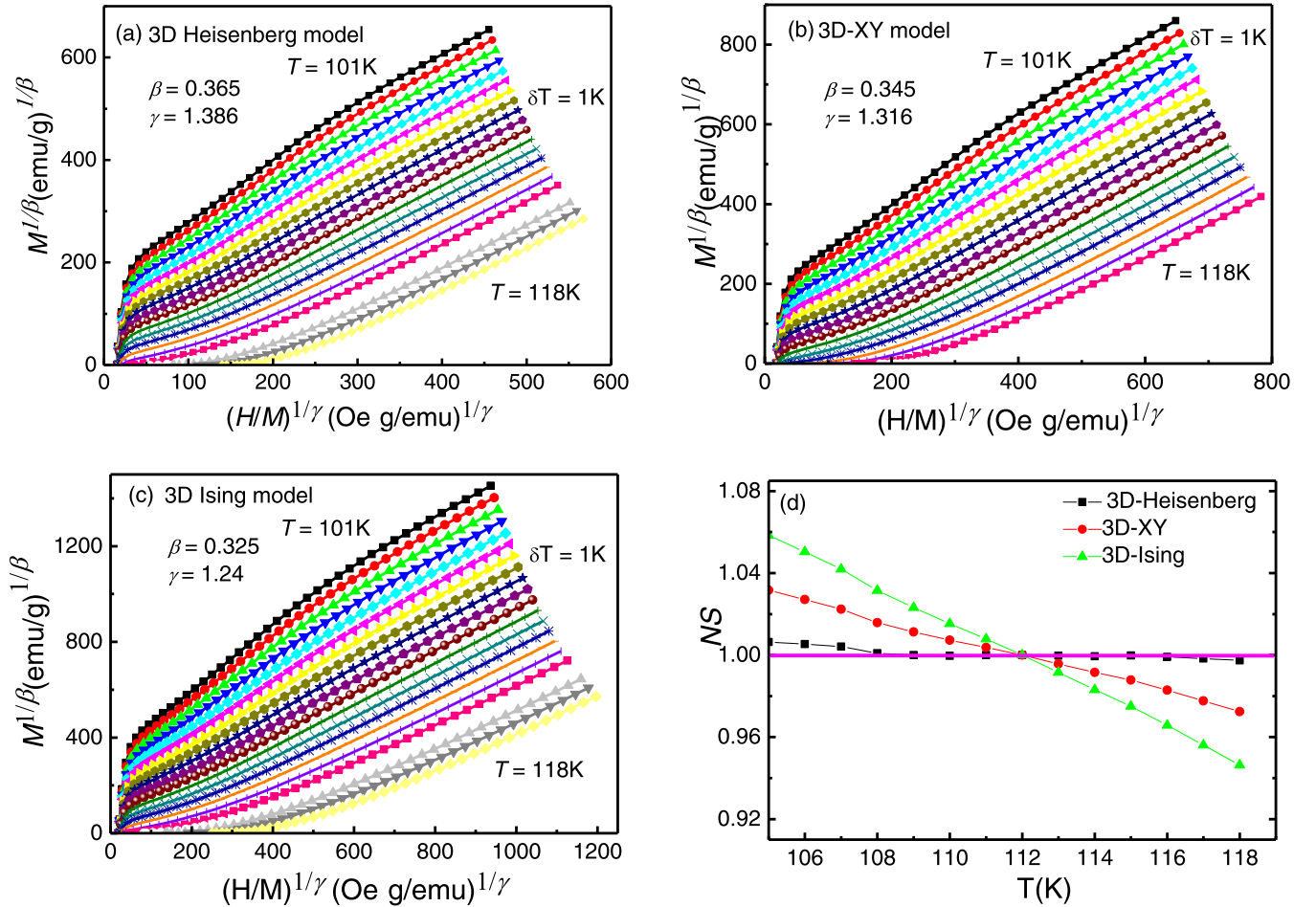
FIG. 5. (a)–(c) The modified Arrott plots at different models: (a) 3D Heisenberg model, (b) 3D XY model, and (c) 3D Ising model. (d) The normalized slopes $NS = S(T)/S(T_C)$ vs temperature for different modes.

hypothesis, in the critical asymptotic region, the magnetic equation can be written as [48]

$$M(H, \varepsilon) = \varepsilon^\beta f_\pm \left(\frac{H}{\varepsilon^{\beta+\gamma}} \right), \quad (6)$$

where f is the scaling function with f_+ for $T > T_C$ and f_- for $T < T_C$. The scaling equation indicates that the plot of $\varepsilon^{-\beta} M(H, \varepsilon)$ vs $\varepsilon^{-(\beta+\gamma)} H$ should produce two universal curves, one for $T > T_C$ and the other for $T < T_C$, if the critical exponents and T_C are reasonable. Therefore, we plot $\varepsilon^{-\beta} M(H, \varepsilon)$ as a function of $\varepsilon^{-(\beta+\gamma)} H$ using the critical exponents and T_C obtained from the Kouvel-Fisher method, which is shown in Fig. 8(a). It is clear that the curves in the higher-field region for all the isothermal magnetization data collapsed into two separated branches. The inset of Fig. 8(a) shows the corresponding ln-ln plot. Similarly, all the points collapse into two curves in the high-field region. In addition, this can be further verified by a more rigorous method using an m^2 vs h/m plot, where the renormalized magnetization $m \equiv \varepsilon^{-\beta} M(H, \varepsilon)$ and the renormalized field $h \equiv \varepsilon^{-(\beta+\gamma)} H$. As shown in Fig. 8(b), all the curves also collapse into two divided branches. Thus, the values of the critical exponents β and γ and the critical temperature T_C obtained by a different method are confirmed to be reliable. The T_C value obtained by the Arrott plot method is lower than that deter-

mined from the magnetic susceptibility experiments, which is a general phenomenon as has been seen in Cr_2Ge_2Te [49]. The obtained critical exponents of La_3MnAs_5 and those of different theoretical models are summarized in Table II, from which it can be seen that the critical behavior in La_3MnAs_5 can be described by the Heisenberg model. It is suggested that short-range spin exchange interaction should dominate the transition in La_3MnAs_5. The critical exponents of the isostructural compound of La_3CrAs_5 are included in Table II as well. The closeness of critical exponents to the chiral XY model implies La_3CrAs_5 should be a frustrated noncollinear ferromagnet.

C. Calculations

To further study the electronic structure and ferromagnetic mechanism in La_3MnAs_5, we performed the first-principles electronic structure calculations. The calculations of total energy for different magnetic structures suggest a ferromagnetic ground state for La_3MnAs_5. Among all the magnetic structure calculations, our calculated magnetic moment on the Mn atom is always around 4.0 μ_B, slightly higher than the measured value of $S = 3.4$. This may arise from the result that our calculation cannot completely rule out the effect of itinerant electrons.
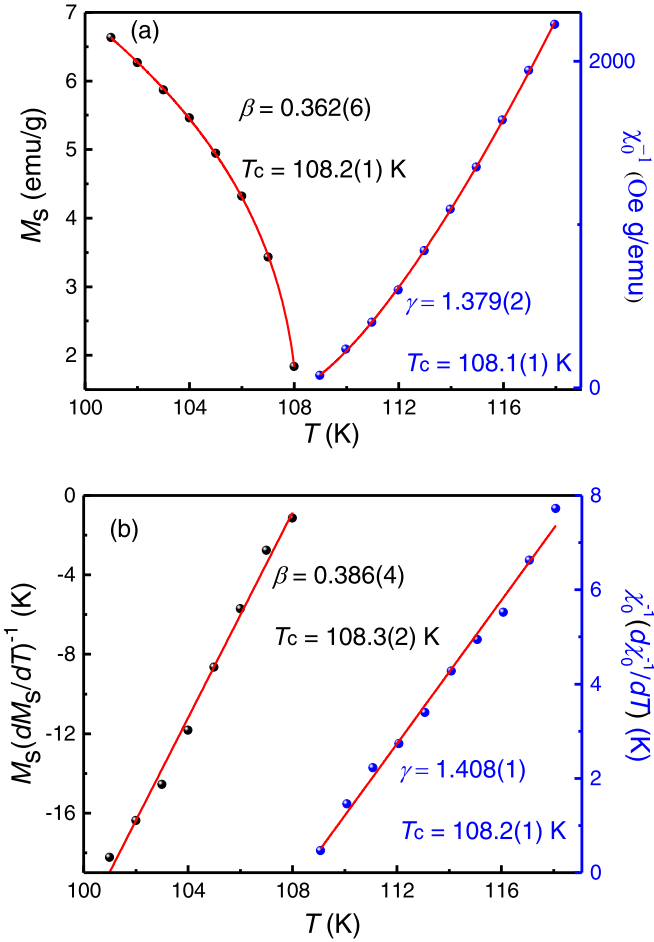
FIG. 6. (a) The spontaneous magnetization $M_S(T)$ (left) and inverse initial susceptibility $\chi_0^{-1}(T)$ (right) vs temperature La$_3$MnAs$_5$. The red is the fitting curves. (b) Kouvel-Fisher plot for $M_S(T)[dM_S(T)/dT]^{-1}$ (left) and $\chi_0^{-1}(T)[d\chi_0^{-1}(T)/dT]^{-1}$ (right) with the solid fitting lines.

FIG. 7. The critical isotherm analysis at 108 K. The inset presents the plot on ln-ln scale with a fitted solid line.

Figure 9(a) shows the calculated spin-polarized electronic structure for La$_3$MnAs$_5$, where the red and blue lines represent the spin-up and spin-down channels, respectively. Figure 9(b) displays the total density of states (DOS). The nonzero DOS distribution around the Fermi level is consistent with the metallic behavior of La$_3$MnAs$_5$ observed by experiments. Figure 9(c) demonstrates the partial orbital DOS of
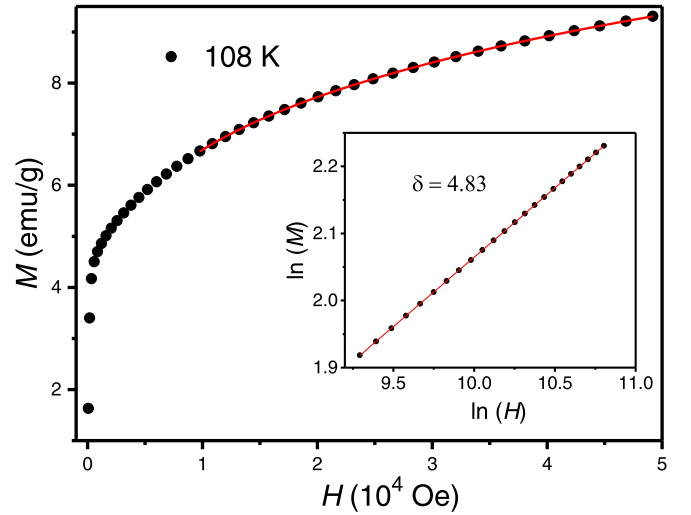
the intermediate La atom (red line), Mn atom (blue line), As1 atom in the MnAs$_6$ chain (purple line), and As2 atom in the As chain (green line), respectively. It can be seen that all the atoms have non-negligible DOS around the Fermi level. In particular, for the Mn atom, nearly all the valence electrons lie in the spin-up channel, implying a spin-polarized state. Figures 10(a)–10(d) display the projected orbital weight of La, Mn, As1, and As2 atoms in the band structure, where the orbital weight is represented by the size of the dots on the band structure and the red/blue dot signals spin-up/down channel.

As shown in Figs. 9(a) and 10(a)–10(d), there are multiple bands crossing the Fermi level, which implies a complex Fermi surfaces (FSs) character in La$_3$MnAs$_5$. Figures 11(a) and 11(b) further display the FSs in the A-Γ-M cut of the Brillouin zone. The FSs with spin-up (red lines) are shown in Fig. 11(a) and the spin-down (blue lines) channel in Fig. 11(b). In brief, these electronic states near the Fermi level can be classified into three types: The first type of FS1 includes 3D + 1D FSs which mainly come from the As1 atomic orbits in the MnAs$_6$ chain, as can be seen with the large orbital weight of As1 with blue dots in Fig. 10(c). Due to the spin polarization by the spin-up Mn ions, these electronic states are slightly spin split. The 3D + 1D FS1 also can be clearly seen

TABLE II. Comparison of critical exponents of La$_3$MnAs$_5$ with different theoretical models and related materials (MAP = modified Arrott plot; KF = Kouvel-Fisher method; CI = critical isotherm analysis).

| Composition	Technique	Reference	T_C (K)	β	γ	δ
La$_3$MnAs$_5$	MAP	This work	108.2(1)	0.362(6)	1.379(2)	4.81[cal]
	KF	This work	108.3(2)	0.386(4)	1.408(1)	4.64[cal]
	CI	This work	108			4.83
La$_3$CrAs$_5$	MAP	[8]	49.9	0.285(6)	1.162(7)	5.07(1)
3D Heisenberg model	Theory	[45]		0.365	1.386	4.8
Chiral XY model	Theory	[8]		0.253	1.135	5.49
Mean field model	Theory	[45]		0.5	1.0	3.0
3D XY model	Theory	[45]		0.345	1.316	4.8
3D Ising model	Theory	[45]		0.325	1.24	4.82
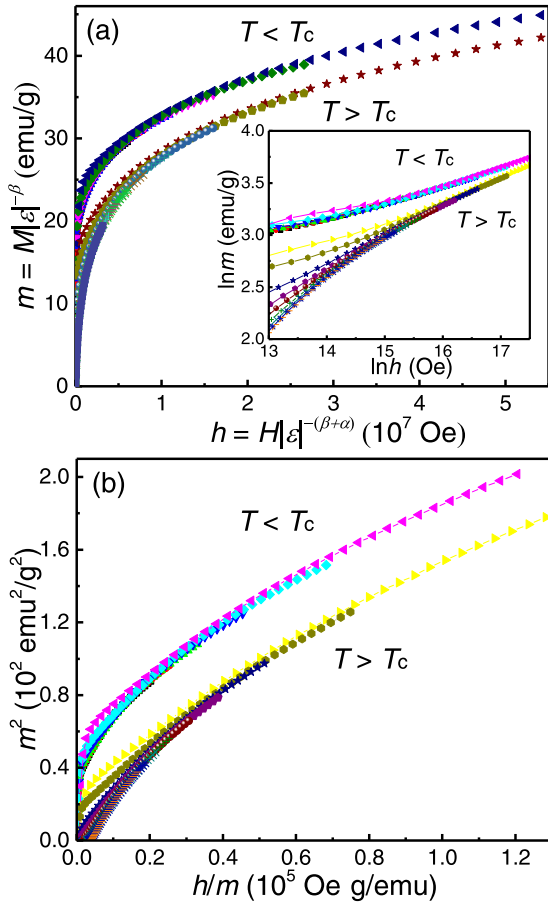
FIG. 8. (a) Scaling plots of renormalized magnetization m vs renormalized field h below and above T_C for La$_3$MnAs$_5$. The inset presents the plot on ln-ln scale. (b) The m^2 vs h/m plot.

FIG. 9. (a) The calculated spin-polarized electronic band structure for La$_3$MnAs$_5$, where the red and blue lines represent spin-up and spin-down channels, respectively. (b), (c) The total and partial orbital density of states (DOS), where the distribution from the La atom, Mn atom, As1 atom in the MnAs$_6$ chain, and the As2 atom in the As chain are represented by the red, blue, purple, and green line, respectively.

in Figs. 11(a) and 11(b), where the flat 1D FSs and closed 3D Fermi sheets are sketched with green dashed lines. The sizes of FS1 between spin-up and spin-down channels are slightly different, demonstrating the small spin-polarized state. The second type (FS2) is a series of 3D Fermi surfaces within a single spin-up channel, which can be easily distinguished by the Mn orbital weight in Fig. 10(b). These electronic states come from the orbital hybridization between the MnAs$_6$ chain and the intermediate La atoms; this orbital hybridization plays an important role in transmitting spin interaction among the MnAs$_6$ spin chains. FS2 is sketched by purple dashed lines in Fig. 11(a) which are missing in the spin-down channel in Fig. 11(b). The last one (FS3) hase two 1D FSs along the Γ-A direction. As shown in Fig. 10(d), these 1D FSs come from the As2 atoms in the As chain and are nearly spin degenerated. The two straight yellow dashed lines in Figs. 11(a) and 11(b) describe the strongly 1D character of this FS3.

To examine the interchain spin coupling strength in the case of the existence of itinerant electrons, we calculated the energy differences between the FM ground state and three AFM ground states of intrachain AFM, interchain striped AFM, and interchain zigzag AFM, the results of which are shown in Table III. By mapping the total energies of the above magnetic configurations to a 3D Heisenberg model with nearest neighbor spin coupling J_{intra} (intrachain) and J_{inter}
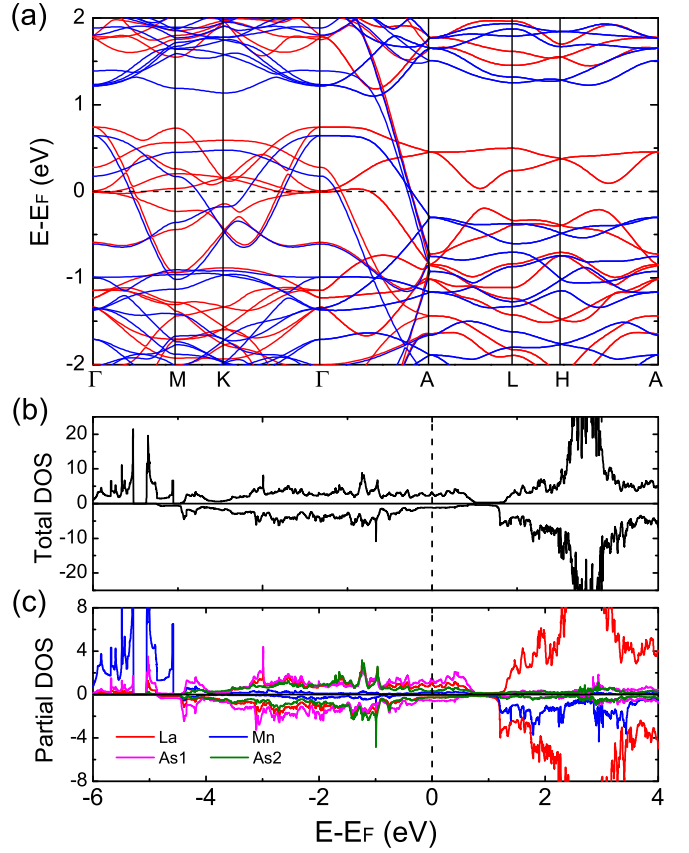
(interchain) and the measured local spin $S = 3.4/2$, we get the $J_{intra} = -6.60$ meV and $J_{inter} = -0.87$ meV with a ratio of $J_{intra}/J_{inter} = 7.59$. It is revealed that in La$_3$MnAs$_5$, although the spin chains are separated by a large distance, the interchain spin coupling is moderate because of the itinerant hybridized electrons, which leads to a high ferromagnetic transition T_C relative with a quasi-1D spin chain system with insulating state.

D. Discussions

For a quasi-1D spin chain system, there are two energy scales of intrachain spin coupling, J_{intra} and interchain spin coupling J_{inter}, and the strength of J_{inter} is usually much weaker than J_{intra} [50]. Due to strong quantum spin fluctuation in

TABLE III. The calculated energy difference ($\Delta E = E_{AFM} - E_{FM}$) between the FM ground state and three AFM ground states of intrachain AFM, interchain stripy AFM, and interchain zigzag AFM.

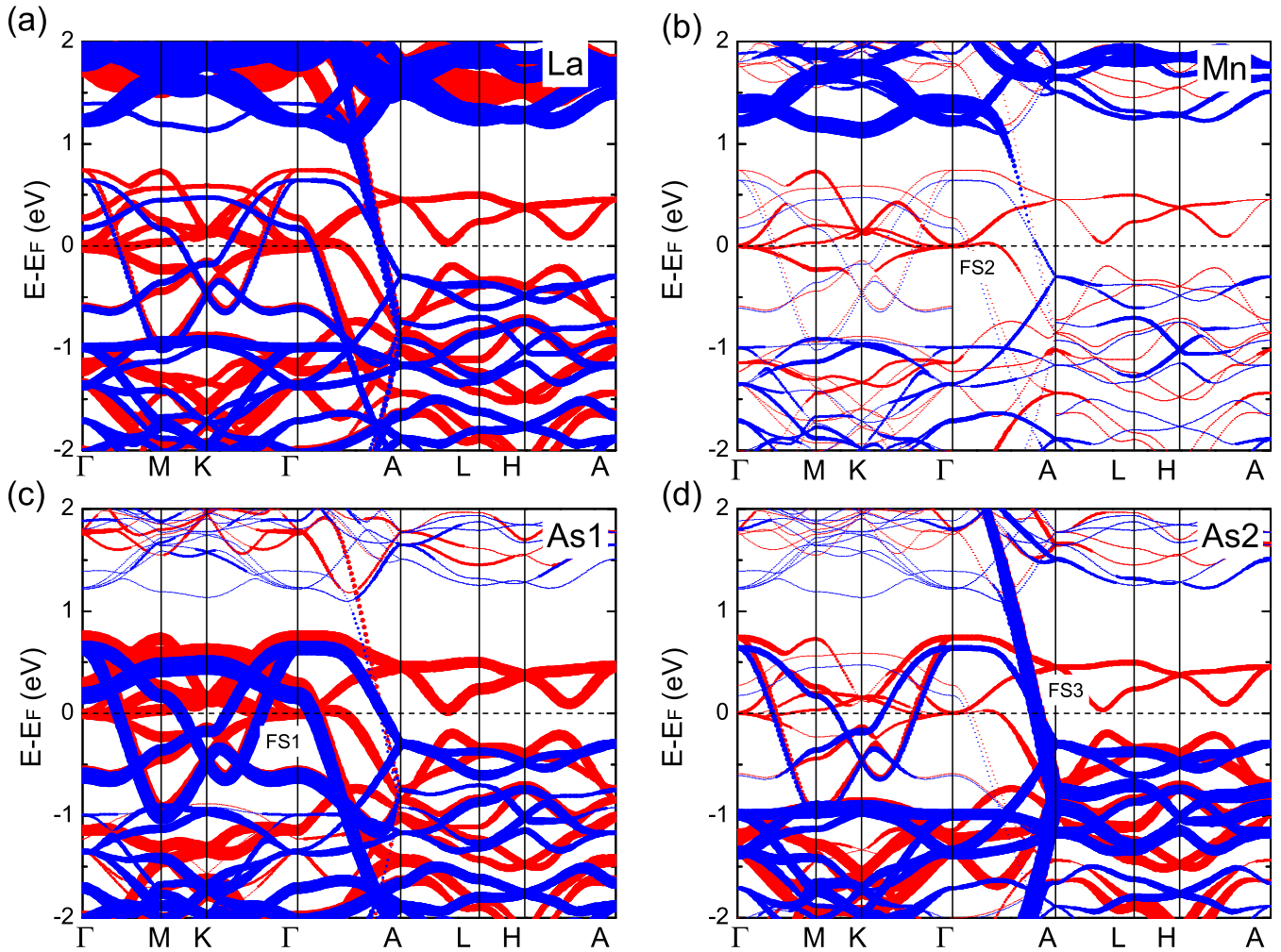| Magnetism state	FM	Intra	Inter (stripy)	Inter (zigzag)
ΔE (meV/Mn)	0.0	64.7	20.1	19.5

FIG. 10. (a)–(d) The projected orbital weight of (a) La, (b) Mn, (c) As1, and (d) As2 atoms on the band structure, where the orbital weight is represented by the size of the dots. The red and blue dots denote spin-up and spin-down channels, respectively.

a dimension-reduced system, J_{inter} governs the LRSO transition while J_{intra} is responsible for the generation of SRSOs
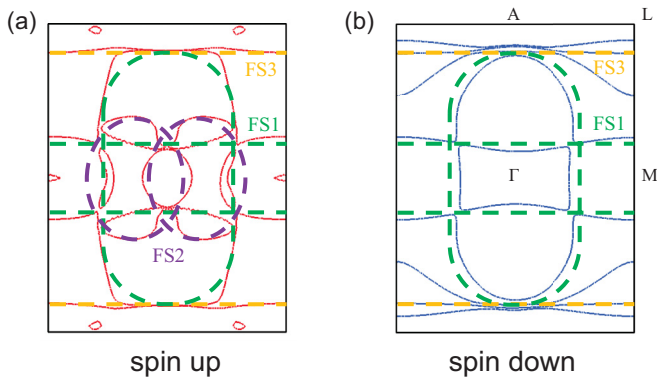

FIG. 11. (a), (b) show the calculated Fermi surface (FS) cut in the A-Γ-M panel of the Brillouin zone for spin-up (red lines) and spin-down (blue lines) channels, respectively. Here we sketched different class of FS by colored dashed lines, where the FS1 (green) and FS3 (yellow) are nearly spin degenerate, while the FS2 (purple) are in single spin channel.

far above the LRSO transition [3]. Many exotic phenomena emerge due to the existence of SRSOs [7,11,13], for example, in $Ba_6Cr_2S_{10}$ [4], no specific heat jump was observed corresponding to the LRSO formation because the development of the SRSOs has already released most of the magnetic entropy before LRSO forms. Besides the 1D magnetic properties related with SRSOs, the reduced moment is another common phenomenon of low-dimensional systems [51,52]. Because partial moments are still disordered below the LRSO temperature due to strong spin fluctuation, the ordered spin moments are generally found to be reduced relative to the fully ordered state. Different from Ba_3MX_5 with insulating state, La_3CrAs_5 has been reported to be metallic although it has a spin-chain structure [7]. It undergoes a LRSO transition at ∼50 K. It is supposed that the interchain coupling J_{inter} should be enhanced via the itinerant electrons, which causes a much higher LRSO temperature than Ba_3MX_5. In addition, La_3CrAs_5 demonstrates typical 1D magnetic properties. The almost invisible kink in the specific heat at 50 K is indicative of very small magnetic entropy change corresponding to the LRSO transition, suggesting the formation of SRSOs far above the LRSO transition. For the same reason, the LRSO transition only causes a very small resistivity change in

La$_3$CrAs$_5$. The fully ordered moment should be 2.3 μ_B per Cr (estimated from the effective moment of 3.1 μ_B per Cr) while the saturated moment at 2 K is reduced by 22% to 1.8 μ_B per Cr, which indicates the strong magnetic fluctuation due to the reduced dimension.

La$_3$MnAs$_5$ is another example which is featured with a well-separated spin chain structure but with a metallic state. La$_3$MnAs$_5$ exhibits 1D magnetic properties as well, although it undergoes a high-temperature LRSO transition. The magnetic susceptibility deviates from CW behavior at ∼170 K, far above the LRSO temperature, suggesting the SRSOs have developed due to the intrachain spin coupling. The $|J_{intra}|$ value can be estimated to be 2.4 meV by the equation $K_B T = \frac{2}{3}z[S(S+1)|J_{intra}|]$, where $z = 2$ is the number of nearest neighbor atoms, $T = 170$ K denotes the SRSOs formation temperature, and the local moment $S = 3.4/2$. The obtained value of J_{intra} is comparable with the theory calculations. Also, because of the formation of SRSOs, the magnetic entropy change at 112 K is only ∼9.5% of the expected value. The saturation moment μ_{sat} at 2 K is reduced to 1.8 μ_B per Mn and the reduction is ∼47% of the fully ordered moment of 3.4 μ_B per Mn. In addition, La$_3$MnAs$_5$ enables us to clearly see how the interchain spins are coupled via itinerant electrons by electric band structure calculations. The electric bands featured with a single spin-up channel near the Fermi level are mixed with Mn, As1 in the MnAs$_6$ chain, and La band components. It is clear that the orbitals of the MnAs$_6$ chain and the intermediate La atoms are hybridized, and the itinerant electrons derived from the orbital hybridization act as the medium to transfer the interaction between local moments.

Now, we compare the differences between La$_3$MnAs$_5$ and La$_3$CrAs$_5$. Since the interchain spin coupling governs the LRSO transition in a quasi-1D spin chain system, a larger J_{inter} implies a higher LRSO temperature. Compared with La$_3$CrAs$_5$, the higher LRSO temperature of 112 K in La$_3$MnAs$_5$ indicates that the interchain spin coupling J_{inter} should be further enhanced via the itinerant electrons. As a result, La$_3$MnAs$_5$ has larger changes of both resistivity and specific heat corresponding to the LRSO transition. It is suggested that La$_3$MnAs$_5$ should have fewer 1D magnetic characteristics relative to La$_3$CrAs$_5$. Surprisingly, the reduction of saturated moment in La$_3$MnAs$_5$ is larger than La$_3$CrAs$_5$ although the former has fewer 1D magnetic characteristics. In addition, the two compounds have different critical behaviors: the 3D Heisenberg model for La$_3$MnAs$_5$ but the chiral XY model for La$_3$CrAs$_5$. For a RKKY magnetic system, whether local spins are coupled ferromagnetically or antiferromagnetically depends on both the electronic DOS near the Fermi level and the distance of local spins. It is

speculated that there should exist severe magnetic frustration in both La$_3$MnAs$_5$ and La$_3$CrAs$_5$ compounds, where the interchain spins are coupled via itinerant electrons. As we know, magnetic frustration usually can lead to the spin glass state [53], noncollinear chiral spin ordering [54], and reduced ordered moment [55]. Therefore, chiral XY type critical behavior observed in La$_3$CrAs$_5$ is suggested to arise from magnetic frustration, while for the 3D Heisenberg type ferromagnet of La$_3$MnAs$_5$, magnetic frustration results in a larger reduction of saturation moment relative to La$_3$CrAs$_5$. La$_3$MnAs$_5$ as well as La$_3$CrAs$_5$ are rare examples which are located in the situation between the usual quasi-1D spin chain system and 3D magnetism, and provide a good chance to study the mechanism of coupling between well-separated local moments via itinerant electrons.

IV. CONCLUSION

In conclusion, a spin-chain compound La$_3$MnAs$_5$ has been synthesized under high-pressure and high-temperature conditions. It crystalizes in a hexagonal structure ($P6_3/mcm$) which consists of MnAs$_6$ chains separated by a large distance, 8.9913 Å. La$_3$MnAs$_5$ exhibits 3D metallic behavior, while it undergoes a ferromagnetic transition at $T_C \sim 112$ K. In spite of the metallic state, the deviation of susceptibility from CW behavior above T_C, reduced ordered moment, and small magnetic entropy change at T_C indicate that La$_3$MnAs$_5$ possesses the properties of quasi-1D spin chains. The magnetic critical behavior can be described with a 3D Heisenberg model. The DFT calculations demonstrate the existence of orbital hybridization between the MnAs$_6$ chain and intermediate La atom around the Fermi level. Our results reveal that the well-separated spin chains in La$_3$MnAs$_5$ are coupled via itinerant electrons. Thus, the interchain spin coupling strength is enhanced and leads to very high T_C relative to the quasi-1D spin chain system with insulating state.

[1] T. Giamarchi, *Quantum Physics in One Dimension* (Oxford University Press, Oxford, UK, 2004).

[2] N. D. Mermin and H. Wagner, Phys. Rev. Lett. **17**, 1133 (1966).

[3] L. J. De Jongh and A. R. Miedema, Adv. Phys. **50**, 947 (2001).

[4] J. Zhang, X. C. Wang, L. Zhou, G. X. Liu, D. T. Adroja, I. Da Silva, F. Demmel, D. Khalyavin, J. Sannigrahi, H. S. Nair, L. Duan, J. F. Zhao, Z. Deng, R. Z. Yu, X. Shen, R. C. Yu, H. Zhao, J. M. Zhao, Y. W. Long, Z. W. Hu *et al.*, Adv. Mater. **34**, 2106728 (2022).

[5] M. Schmitt, P. Moras, G. Bihlmayer, R. Cotsakis, M. Vogt, J. Kemmer, A. Belabbes, P. M. Sheverdyaeva, A. K. Kundu, C. Carbone, S. Blugel, and M. Bode, Nat. Commun. **10**, 2610 (2019).

[6] P. Ferstl, L. Hammer, C. Sobel, M. Gubo, K. Heinz, M. A. Schneider, F. Mittendorfer, and J. Redinger, Phys. Rev. Lett. **117**, 046101 (2016).

[7] L. Duan, X. C. Wang, F. Y. Zhan, J. Zhang, Z. W. Hu, J. F. Zhao, W. M. Li, L. P. Cao, Z. Deng, R. Z. Yu, H.-J. Lin,

C.-T. Chen, R. Wang, and C. Q. Jin, Sci. China Mater. **63**, 1750 (2020).

[8] L. Duan, X. C. Wang, J. Zhang, J. F. Zhao, Z. W. Zhao, C. J. Xiao, C. L. Guan, S. Wang, L. P. Shi, J. L. Zhu, and C. Q. Jin, J. Alloys Compd. **905**, 164214 (2022).

[9] L. Duan, J. Zhang, X. C. Wang, J. F. Zhao, L. P. Cao, W. M. Li, Z. Deng, R. Z. Yu, Z. Li, and C. Q. Jin, J. Alloys Compd. **831**, 154697 (2020).

[10] J. Zhang, A. C. Komarek, M. Jin, X. C. Wang, Y. T. Jia, J. F. Zhao, W. M. Li, Z. W. Hu, W. Peng, X. Wang, L. H. Tjeng, Z. Deng, R. Z. Yu, S. M. Feng, S. J. Zhang, M. Liu, Y.-F. Yang, H.-J. Lin, C.-T. Chen, X. D. Li *et al.*, Phys. Rev. Mater. **5**, 054606 (2021).

[11] J. Zhang, L. Duan, Z. Wang, X. C. Wang, J. F. Zhao, M. L. Jin, W. M. Li, C. L. Zhang, L. P. Cao, Z. Deng, Z. W. Hu, S. Agrestini, M. Valvidares, H. J. Lin, C. T. Chen, J. L. Zhu, and C. Q. Jin, Inorg. Chem. **59**, 5377 (2020).

[12] J. Zhang, Y. T. Jia, X. C. Wang, Z. Li, L. Duan, W. M. Li, J. F. Zhao, L. P. Cao, G. Y. Dai, Z. Deng, S. J. Zhang, S. M. Feng, R. Z. Yu, Q. Q. Liu, J. P. Hu, J. L. Zhu, and C. Q. Jin, NPG Asia Mater. **11**, 60 (2019).

[13] J. Zhang, M. Liu, X. C. Wang, K. Zhao, L. Duan, W. M. Li, J. F. Zhao, L. P. Cao, G. Y. Dai, Z. Deng, S. M. Feng, S. J. Zhang, Q. Q. Liu, Y. F. Yang, and C. Q. Jin, J. Phys.: Condens. Matter **30**, 214001 (2018).

[14] J. Zhang, R. Su, X. C. Wang, W. M. Li, J. F. Zhao, Z. Deng, S. J. Zhang, S. M. Feng, Q. Q. Liu, H. Z. Zhao, P. F. Guan, and C. Q. Jin, Inorg. Chem. Front. **4**, 1337 (2017).

[15] L. Duan, X.-C. Wang, J. Zhang, J.-F. Zhao, L.-P. Cao, W.-M. Li, R.-Z. Yu, Z. Deng, and C.-Q. Jin, Chin. Phys. B **29**, 036102 (2020).

[16] J. Zhang, M. L. Jin, X. Li, X. C. Wang, J. F. Zhao, Y. Liu, L. Duan, W. M. Li, L. P. Cao, B. J. Chen, L. J. Wang, F. Sun, Y. G. Wang, L. X. Yang, Y. M. Xiao, Z. Deng, S. M. Feng, C. Q. Jin, and J. L. Zhu, Chin. Phys. Lett. **37**, 087106 (2020).

[17] L. Duan, X. C. Wang, J. Zhang, J. F. Zhao, W. M. Li, L. P. Cao, Z. W. Zhao, C. J. Xiao, Y. Ren, S. Wang, J. L. Zhu, and C. Q. Jin, Chin. Phys. B **30**, 106101 (2021).

[18] S. H. D. Moore, L. Deakin, M. J. Ferguson, and A. Mar, Chem. Mater. **14**, 4867 (2002).

[19] O. Y. Zelinska and A. Mar, Inorg. Chem. **47**, 297 (2008).

[20] T. Murakami, T. Yamamoto, F. Takeiri, K. Nakano, and H. Kageyama, Inorg. Chem. **56**, 5041 (2017).

[21] J. F. Zhao, J. C. Gao, W. M. Li, Y. T. Qian, X. D. Shen, X. Wang, X. Shen, Z. W. Hu, C. Dong, Q. Z. Huang, L. P. Cao, Z. Li, J. Zhang, C. W. Ren, L. Duan, Q. Q. Liu, R. C. Yu, Y. Ren, S.-C. Weng, H.-J. Lin *et al.*, Nat. Commun. **12**, 747 (2021).

[22] Z. W. Li, X. He, C. L. Zhang, X. C. Wang, S. J. Zhang, Y. T. Jia, S. M. Feng, K. Lu, J. F. Zhao, J. Zhang, B. S. Min, Y. W. Long, R. C. Yu, L. H. Wang, M. Y. Ye, Z. S. Zhang, V. Prakapenka, S. Chariton, P. A. Ginsberg, J. Bass *et al.*, Nat. Commun. **13**, 2863 (2022).

[23] C. L. Zhang, X. He, Z. W. Li, S. J. Zhang, S. M. Feng, X. C. Wang, R. C. Yu, and C. Q. Jin, Sci. Bull. **67**, 907 (2022).

[24] C. Q. Jin, S. Adachi, X. J. Wu, H. Yamauchi, and S. Tanaka, Phys. C (Amsterdam) **223**, 238 (1994).

[25] P. Hohenberg and W. Kohn, Phys. Rev. **136**, B864 (1964).

[26] W. Kohn and L. J. Sham, Phys. Rev. **140**, A1133 (1965).

[27] P. Giannozzi, S. Baroni, N. Bonini, M. Calandra, R. Car, C. Cavazzoni, D. Ceresoli, G. L. Chiarotti, M. Cococcioni, I. Dabo, A. Dal Corso, S. De Gironcoli, S. Fabris, G. Fratesi, R. Gebauer, U. Gerstmann, C. Gougoussis, A. Kokalj, M. Lazzeri, L. Martin-Samos *et al.*, J. Phys.: Condens. Matter **21**, 395502 (2009).

[28] A. Dal Corso, Comput. Mater. Sci. **95**, 337 (2014).

[29] J. P. Perdew, K. Burke, and M. Ernzerhof, Phys. Rev. Lett. **77**, 3865 (1996).

[30] S. L. Dudarev, G. A. Botton, S. Y. Savrasov, C. J. Humphreys, and A. P. Sutton, Phys. Rev. B **57**, 1505 (1998).

[31] B. C. Gong, H. C. Yang, J. F. Zhang, K. Liu, and Z. Y. Lu, Phys. Rev. B **104**, 075133 (2021).

[32] J. H. Li, Y. Li, S. Q. Du, Z. Wang, B. L. Gu, S. C. Zhang, K. He, W. H. Duan, and Y. Xu, Sci. Adv. **5**, eaaw5685 (2019).

[33] C. Gauvin-Ndiaye, T. E. Baker, P. Karan, E. Masse, M. Balli, N. Brahiti, M. A. Eskandari, P. Fournier, A. M. S. Tremblay, and R. Nourafkan, Phys. Rev. B **98**, 125132 (2018).

[34] G. Bollore, M. J. Ferguson, R. W. Hushagen, and A. Mar, Chem. Mater. **7**, 2229 (1995).

[35] C. Mitra, Z. Hu, P. Raychaudhuri, S. Wirth, S. I. Csiszar, H. H. Hsieh, H. J. Lin, C. T. Chen, and L. H. Tjeng, Phys. Rev. B **67**, 092404 (2003).

[36] A. N. Vasiliev, O. S. Volkova, L. S. Lobanovskii, I. O. Troyanchuk, Z. Hu, L. H. Tjeng, D. I. Khomskii, H. J. Lin, C. T. Chen, N. Tristan, F. Kretzschmar, R. Klingeler, and B. Buchner, Phys. Rev. B **77**, 104442 (2008).

[37] T. Burnus, Z. Hu, H. H. Hsieh, V. L. J. Joly, P. A. Joy, M. W. Haverkort, H. Wu, A. Tanaka, H. J. Lin, C. T. Chen, and L. H. Tjeng, Phys. Rev. B **77**, 125124 (2008).

[38] J. W. Simonson, Z. P. Yin, M. Pezzoli, J. Guo, J. Liu, K. Post, A. Efimenko, N. Hollmann, Z. Hu, H. J. Lin, C. T. Chen, C. Marques, V. Leyva, G. Smith, J. W. Lynn, L. L. Sun, G. Kotliar, D. N. Basov, L. H. Tjeng *et al.*, Proc. Natl. Acad. Sci. USA **109**, E1815 (2012).

[39] J. Q. Yan, J. S. Zhou, J. G. Cheng, J. B. Goodenough, Y. Ren, A. Llobet, and R. J. Mcqueeney, Phys. Rev. B **84**, 214405 (2011).

[40] Z. Deng, C. Q. Jin, Q. Q. Liu, X. C. Wang, J. L. Zhu, S. M. Feng, L. C. Chen, R. C. Yu, C. Arguello, T. Goko, F. L. Ning, J. S. Zhang, Y. Y. Wang, A. A. Aczel, T. Munsie, T. J. Williams, G. M. Luke, T. Kakeshita, S. Uchida, W. Higemoto *et al.*, Nat. Commun. **2**, 422 (2011).

[41] K. Zhao, Z. Deng, X. C. Wang, W. Han, J. L. Zhu, X. Li, Q. Q. Liu, R. C. Yu, T. Goko, B. Frandsen, L. Liu, F. L. Ning, Y. J. Uemura, H. Dabkowska, G. M. Luke, H. Luetkens, E. Morenzoni, S. R. Dunsiger, A. Senyshyn, P. Boni *et al.*, Nat. Commun. **4**, 1442 (2013).

[42] T. Dietl, Nat. Mater. **9**, 965 (2010).

[43] J. S. Kouvel and M. E. Fisher, Phys. Rev. **136**, A1626 (1964).

[44] H. E. Stanley, *Introduction to phase transition and critical phenomena* (Oxford University Press, London, 1971).

[45] S. N. Kaul, J. Magn. Magn. Mater. **53**, 5 (1985).

[46] S. K. Banerjee, Phys. Lett. **12**, 16 (1964).

[47] A. K. Pramanik and A. Banerjee, Phys. Rev. B **79**, 214426 (2009).

[48] B. Widom, J. Chem. Phys. **43**, 3892 (1965).

[49] Y. Liu and C. Petrovic, Phys. Rev. B **96**, 054406 (2017).

[50] M. F. Collins and O. A. Petrenko, Can. J. Phys. **75**, 605 (1997).

[51] H. J. Schulz, Phys. Rev. Lett. **77**, 2790 (1996).

[52] I. Tsukada, Y. Sasago, K. Uchinokura, A. Zheludev, S. Maslov, G. Shirane, K. Kakurai, and E. Ressouche, Phys. Rev. B **60**, 6601 (1999).

[53] J. S. Gardner, M. J. P. Gingras, and J. E. Greedan, Rev. Mod. Phys. **82**, 53 (2010).

[54] A. O. Leonov and M. Mostovoy, Nat. Commun. **6**, 8275 (2015).

[55] E. Lhotel, S. Petit, S. Guitteny, O. Florea, M. C. Hatnean, C. Colin, E. Ressouche, M. R. Lees, and G. Balakrishnan, Phys. Rev. Lett. **115**, 197202 (2015).